

Elastic scattering, transfer reactions, and fission induced by ^{16}O ions on ^{181}Ta and ^{208}Pb †

F. Videbæk,* R. B. Goldstein, L. Grodzins, and S. G. Steadman

Laboratory for Nuclear Science, Massachusetts Institute of Technology, Cambridge, Massachusetts 02139

T. A. Belote

University of Massachusetts, Boston, Massachusetts 02116

J. D. Garrett*

Brookhaven National Laboratory, Upton, New York 11973

(Received 7 July 1976)

Total cross sections for the quasielastic and fission channels in reactions of ^{16}O on ^{181}Ta and ^{208}Pb were measured as a function of the incident energy near the Coulomb barrier. For ^{208}Pb , the fission and quasielastic components account for essentially all of the total reaction cross sections as deduced from the elastic scattering. However, for ^{181}Ta , the fission and quasielastic components account for only about 25% of the total cross section as deduced from elastic scattering. The fission fragment angular distributions for ^{208}Pb are analyzed with a simple statistical approach yielding an effective moment of inertia at the saddle point compatible with the liquid-drop-model prediction. Fission excitation functions for ^{181}Ta are described reasonably well by a statistical evaporation code.

NUCLEAR REACTIONS Ta(^{16}O , ^{16}O), (^{16}O , ^{17}O), (^{16}O , ^{15}N), (^{16}O , C), (^{16}O , f), $E_L=83, 90, 96$ MeV. ^{208}Pb (^{16}O , ^{16}O), (^{16}O , ^{17}O), (^{16}O , ^{15}N), (^{16}O , C) $E_L=80, 83, 88, 90, 96, 102$ MeV, measured $\sigma(\theta, E)$. Ta(^{16}O , f) $E_L=77-102$ MeV, measured $\sigma(E)$; deduced optical-model parameters, total reaction cross sections; enriched targets.

I. INTRODUCTION

Systematic studies of the competition of the various processes which contribute to the total reaction cross sections are of considerable importance in understanding the dynamics of heavy-ion collisions.¹⁻³ However, most heavy-ion induced reaction studies have concentrated on specific transitions populating individual final states and on spectroscopy resulting from γ and particle deexcitation of the intermediate system. Such studies usually have not been especially concerned with the gross properties of the reaction cross section leading to various quasielastic channels (inelastic scattering and few nucleon transfer) or the formation and deexcitation of a compound system (evaporation residues and, for heavy systems, fission).

The present paper reports systematic, high resolution elastic, quasielastic, and fission data for ^{16}O ions on ^{181}Ta and ^{208}Pb targets at incident energies from the Coulomb barrier up to ~ 20 MeV above the barrier. In Secs. II and III the experimental procedure and the data are discussed. The systematics of the present elastic scattering data and existing $^{16}\text{O}+^{208}\text{Pb}$ elastic data⁴⁻⁶ are discussed in Sec. IV in terms of optical- and strong-absorption-model analyses. In Sec. V the quasielastic and fission cross sections are

discussed together with the total reaction cross section obtained from the optical-model analysis of the elastic data. The fission-fragment angular distributions and the resulting estimates of the saddle point moments of inertia, determined from the deviations from $(\sin\theta)^{-1}$ of the $^{16}\text{O}+^{208}\text{Pb}$ data, are discussed in Sec. VI. The excitation functions of the fission fragments are discussed in Sec. VII in terms of the variation of the rotating liquid-drop fission barrier as a function of angular momentum,⁷ and the work is summarized in Sec. VIII.

II. EXPERIMENTAL METHODS

The ^{16}O beams in the energy range of 77 to 102 MeV were produced at the three stage MP tandem accelerator facility at Brookhaven National Laboratory. Beam intensities were typically of the order of 50–200 nA. Targets of $\sim 100-300$ $\mu\text{g}/\text{cm}^2$ of natural Ta (rolled or evaporated on ~ 20 $\mu\text{g}/\text{cm}^2$ C backing) and ^{208}Pb (99.1% enrichment) evaporated onto ~ 20 $\mu\text{g}/\text{cm}^2$ carbon backings were used for the bombardments.

The scattered particles and reaction products were identified using silicon surface barrier detector telescopes. The forward angle data were obtained using a telescope consisting of a 32 μm ΔE detector and a 60 μm E detector. The 32 μm

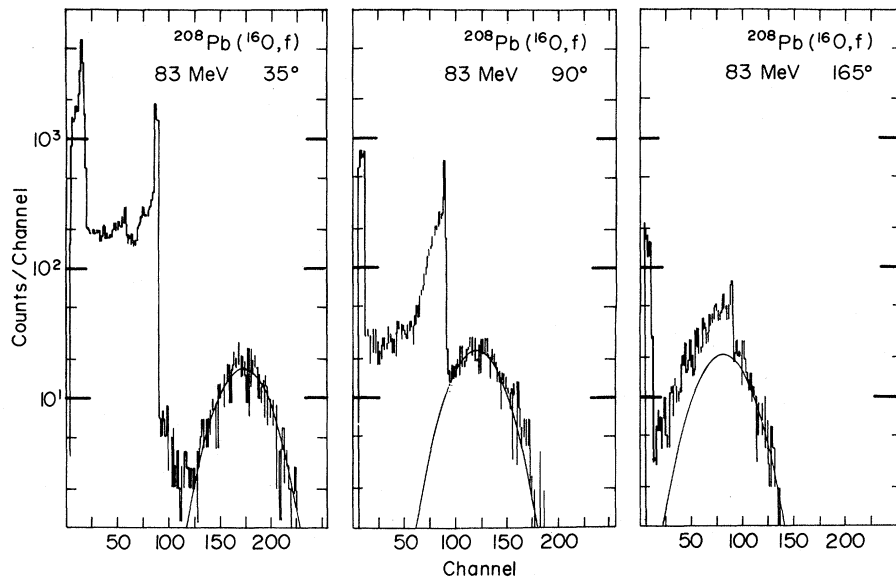


FIG. 1. Energy spectra of the reaction products of $^{16}\text{O} + ^{208}\text{Pb}$ which were stopped in the $32\ \mu\text{m}\ \Delta E$ detector of a two-detector telescope. These spectra corresponding to an ^{16}O incident energy of 83 MeV and measured at laboratory angles of 35° , 90° , and 165° were obtained in anticoincidence with events in the E detector of the telescope. The broad bump at higher energy is attributed to fission. Contributions from low-energy ^{16}O stopped in the ΔE detector are observed below channel 90. The difficulty in distinguishing the fission events from the low-energy ^{16}O events is evident in the 165° spectrum. The solid curves are Gaussian fits to the fission groups.

ΔE detector is thick enough to stop the fission fragments emitted in the reaction, while ^{16}O ions deposit a maximum of 35 MeV in this detector. Fission spectra were obtained from the ΔE detector using the E detector to give a reject signal. For the back angle scattering data, and in particular at incident energies close to the Coulomb barrier, the energies of the fission fragments emitted are low and there is a large background of particles stopped in the ΔE detector corresponding to beam related low-energy ^{16}O events. This is demonstrated in Fig. 1, which shows typical fission spectra obtained by this method. Therefore, to measure this cross section reliably, a three-detector counter telescope consisting of a $9\ \mu\text{m}\ \Delta E_1$, a $15\ \mu\text{m}\ \Delta E_2$ and a $60\ \mu\text{m}\ E$ solid state detector was used. By using the third detector for rejecting light-ion events, the fission fragments can be uniquely discriminated from lighter particles by the energy signal in the first detector. For comparison, a fission spectrum obtained using this setup is shown in Fig. 2.

The elastically scattered particles and few nucleon transfer-reaction products were measured using the same detector telescope in a conventional coincidence mode. For the three-detector telescope the signals from the two thin detectors were added and treated as a single ΔE signal. The ΔE detectors were sufficiently thin to detect

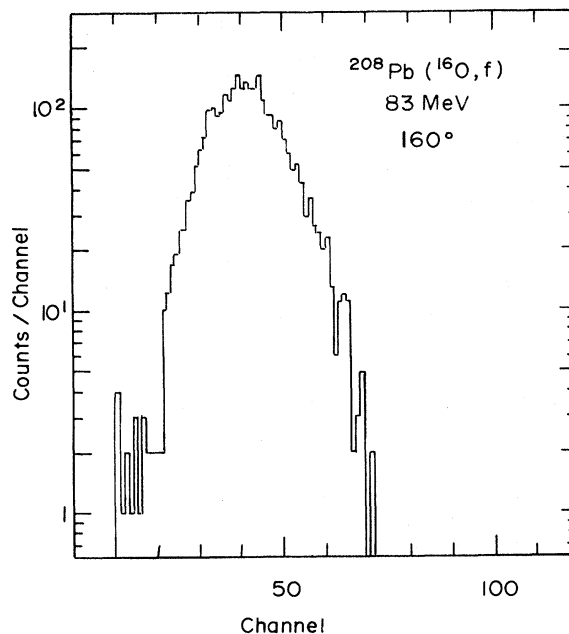


FIG. 2. Fission energy spectrum for $^{16}\text{O} + ^{208}\text{Pb}$ at $E(^{16}\text{O}) = 83\ \text{MeV}$ and $\theta_L = 160^\circ$ obtained with the three-detector telescope as described in the text. The difficulty in distinguishing the fission events from the low-energy ^{16}O events (illustrated in Fig. 1) has been removed by particle identification in the first two detectors of the telescope.

46 MeV ^{20}Ne . The various signals were fed into the Brookhaven Sigma 7 on-line computer and displayed as two-dimensional spectra typically of 128×256 channels. The yield of the elastic scattering in an additional Si detector placed at $\sim 20^\circ$ was used to normalize between the individual runs.

The energy of the heavy particles was calibrated initially using a ^{252}Cf fission source mounted on a thin backing (as described in Ref. 8) and later by elastically scattering 100 MeV ^{79}Br and ^{127}I ions from a thin Au target. The calibration for the light particles was obtained from the elastic scattering of ^{16}O by the Ta and Pb targets.

An energy resolution, typically 400 keV and mainly determined by the target thickness and angular openings of the detectors, was obtained for the light particles. The separation between the various reaction products with different Z was excellent (see Fig. 3). Groups belonging to different isotopes of the same element, e.g., ^{16}O and ^{17}O , were apparent in the two-dimensional spectra, but separated spectra of each group generally were not extracted. The energy spectra of the various groups were projected from the two-dimensional ΔE versus E spectra. Spectra for the quasielastic oxygen channel, which includes inelastic scattering as well as one-neutron transfer and two-neutron transfer reactions were obtained from the oxygen group by subtracting the background due to the elastic tail. Typical spectra for some of the groups in the $^{16}\text{O} + \text{Ta}$ reaction at 96 MeV are shown in Fig. 4. At the incident energies of the present study, which are just above the Coulomb barrier, the angle corresponding to

a grazing collision is large. Therefore, the groups emerging from light target impurities can be identified easily and cause no problems except at the most forward angles where the quasielastic cross sections of interest are very small. The term quasielastic is an appropriate description for the inelastic scattering and transfer reactions for several reasons: The incident energies are close to the barrier height, and deep inelastic phenomena are negligible; the Q values involved in the reactions are generally small, and the angular distributions are typical of grazing collisions.

III. EXPERIMENTAL DATA

Angular distributions were measured in intervals of $5\text{--}10^\circ$ over the angular range of 30 to 160° in the laboratory system. Data were obtained at beam energies of 83, 90, and 96 MeV for the ^{181}Ta target and of 80, 83, 88, 90, 96, and 102 MeV for the ^{208}Pb target. Absolute cross sections for the elastic scattering were established by assuming that the experimental cross section at the most forward angles is the Rutherford cross section. Differential cross sections for the various transfer-reaction products were obtained from the corresponding yield integrated over energy and normalized to the absolute elastic cross section. Due to the background subtraction, the uncertainties in the cross section for the quasielastic oxygen channels are larger than for the other channels. In the case of ^{181}Ta the resolution was not sufficient to separate the inelastic groups for the states of ^{181}Ta below an excitation energy of 1.5 MeV.

Typical angular distributions for the ^{181}Ta and ^{208}Pb targets are displayed in Figs. 5–8. Total cross sections were obtained by integrating the differential cross sections over angle

$$\sigma = 2\pi \int_0^\pi \left(\frac{d\sigma}{d\Omega} \right)_L \sin\theta_L d\theta_L. \quad (1)$$

The angular distributions were extrapolated towards larger and smaller angles, assuming a nonrising differential cross section. At the most forward angle at the highest energies the reaction products from C and O impurities in the target contribute to the differential cross section and the data contain no indication that the products from Ta and Pb should be forward peaked at the measured energies. Because the $\sin\theta_L$ factor is so dominant at the angular extremes, 90% or more of the total cross section is obtained from the angular range covering the actual data. For example, if one were to increase the extrapolated

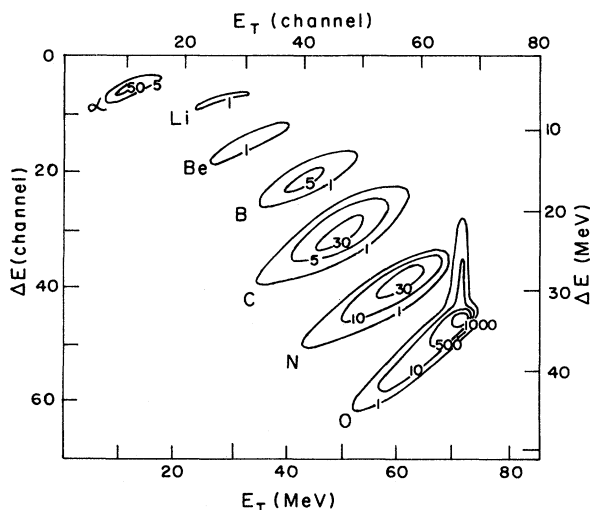


FIG. 3. Contour plot of the reaction products for 90 MeV $^{16}\text{O} + ^{181}\text{Ta}$, detected at 90° in the laboratory with the two-detector counter telescope as described in the text. The energy scales are approximate.

value at 0° by two orders of magnitude, the total cross section is increased by at most 5% and usually much less. The integrated cross sections are given in Table I.

The number of counts for the fission groups measured with the two-detector telescopes was

obtained from the area under a Gaussian peak fitted to the part of the spectrum which did not contain the low-energy oxygen stopped in the E detector. The cross sections obtained in this way agreed with those of the much cleaner spectra from the three-detector telescopes. (Compare

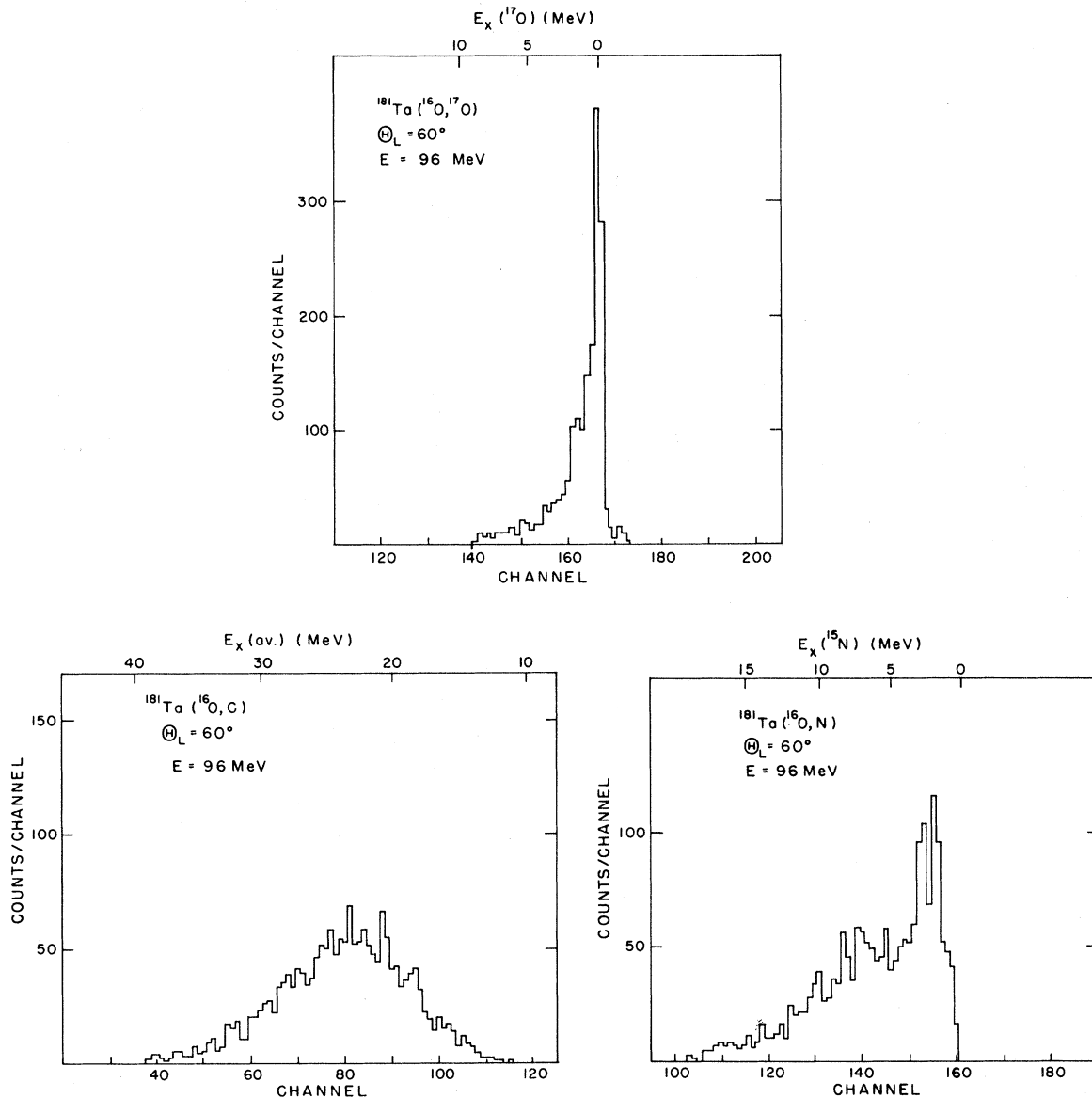


FIG. 4. ^{17}O , N, and C energy spectra for 96 MeV ^{16}O incident on ^{181}Ta obtained at a laboratory angle of 60° . A ^{17}O and a ^{15}N excitation energy scale is shown with the O and N spectra. Since no one C isotope dominates the C group (see text), an excitation energy scale which is the average of ^{12}C and ^{14}C is shown with the C spectra. The ground state Q values corresponding to ^{12}C , ^{13}C , and ^{14}C exit channels are -9.375 , -12.214 , and -10.398 MeV, respectively. The dominant cross sections move to more negative Q values (higher excitation energies) with increasing number of protons transferred. In the O and N spectra a few discrete states contribute a large fraction of the cross section; however, in the C spectrum the strength is concentrated in a large "bump" of overlapping states at a very high excitation in the final systems. Similar systematics were observed at other incident energies and angles and for the corresponding reactions on the ^{208}Pb target.

Figs. 1 and 2.) The center-of-mass differential cross sections were calculated from the laboratory cross section in a manner described in Ref. 9 using the transformation parameter $\chi^2 = v_{c.m.}/v_f$ where $v_{c.m.}$ is the velocity of the center-of-mass system and v_f the average velocity of the fission fragment. This parameter was determined by fitting the measured laboratory mean kinetic energies E_L to an expression of the form

$$E_L = E_{c.m.}(1 + \chi + 2\chi^2 \cos\theta), \quad (2)$$

where $E_{c.m.}$ is the mean kinetic energy of the fission fragments and θ the center-of-mass scattering angle. Examples of such a fit are shown in Fig. 9. The resulting angular distributions for the fission fragments are displayed in Figs. 10 and 11. The total fission cross section obtained by integration of the angular distributions are given in Table I.

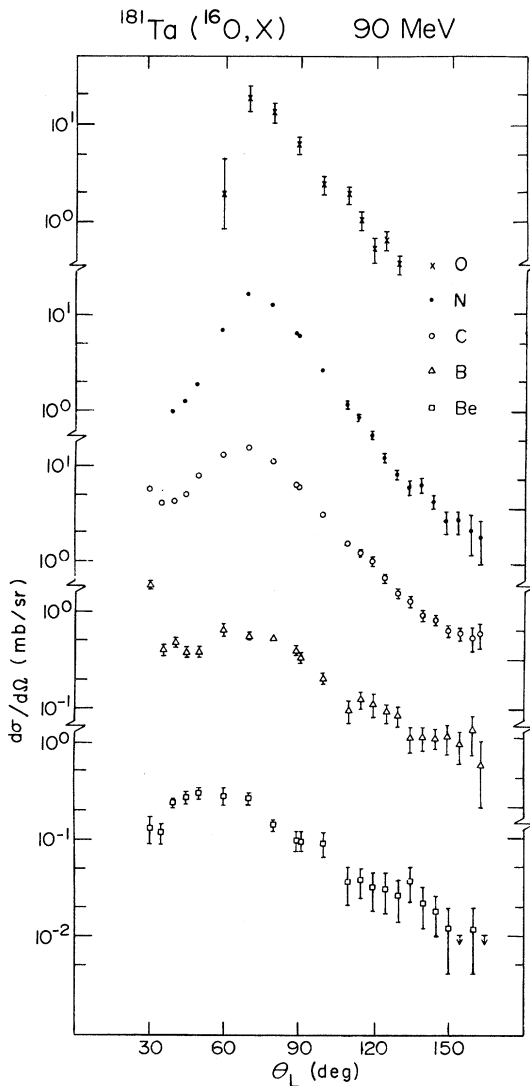


FIG. 5. Angular distributions corresponding to the total energy integrated yield in the O, N, C, B, and Be exit channels for 90 MeV ^{16}O incident on ^{181}Ta . The O channel does not include inelastic scattering to states below 1.5 MeV excitation, since such transitions were not resolved from the elastic scattering. The peak in the C angular distribution is broader than the corresponding peak in the N angular distribution, and such a peak is nearly lost in the B and Be angular distributions.

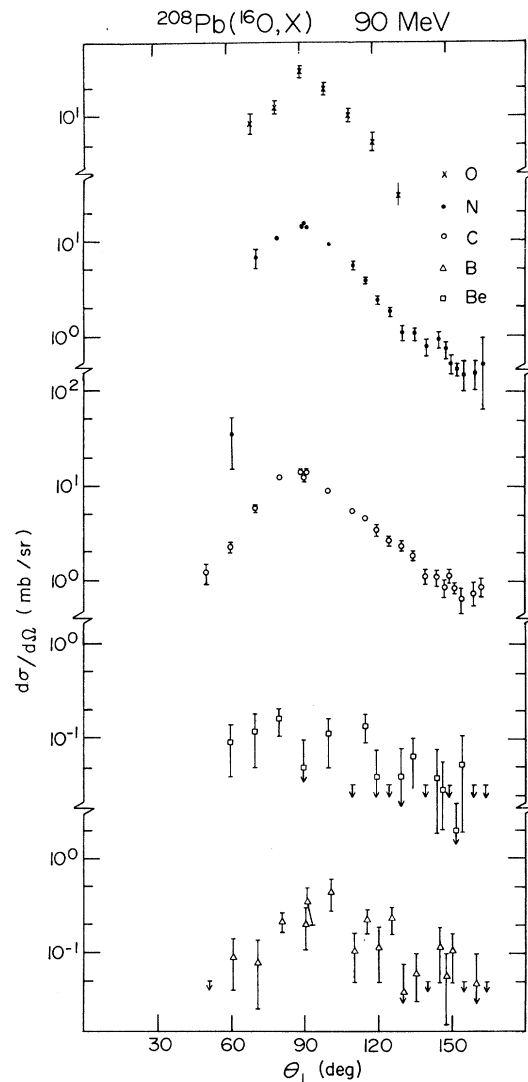


FIG. 6. Angular distributions corresponding to the total energy integrated yield in the O, N, C, B, and Be exit channels for 90 MeV ^{16}O incident on ^{208}Pb . The O channel includes the total cross section for inelastic scattering as well as the transfer reaction cross section. The peak observed in the C angular distribution is broader than the corresponding peaks in the N and O angular distributions.

An excitation function for the fission products emerging in the ^{16}O reaction with ^{181}Ta was measured at energies from 77 to 102 MeV in steps of 1 or 2 MeV. The fission cross section was measured at laboratory angles of 77° and 160° , corresponding to 90° and 165° in the center-of-mass system. From the three angular distributions measured at 83, 90, and 96 MeV the values of $\sigma(165^\circ)/\sigma(90^\circ)$ and $\sigma_f/\sigma(90^\circ)$ were obtained. For all other incident energies, from the measured cross section at 90° (c.m.) and the ratio of $\sigma(165^\circ)/\sigma(90^\circ)$, the total fission cross sections were established by finding the appropriate ratio of $\sigma_f/\sigma(90^\circ)$ by interpolating to the known value from the angular distributions. The corrections introduced to the cross sections by using this

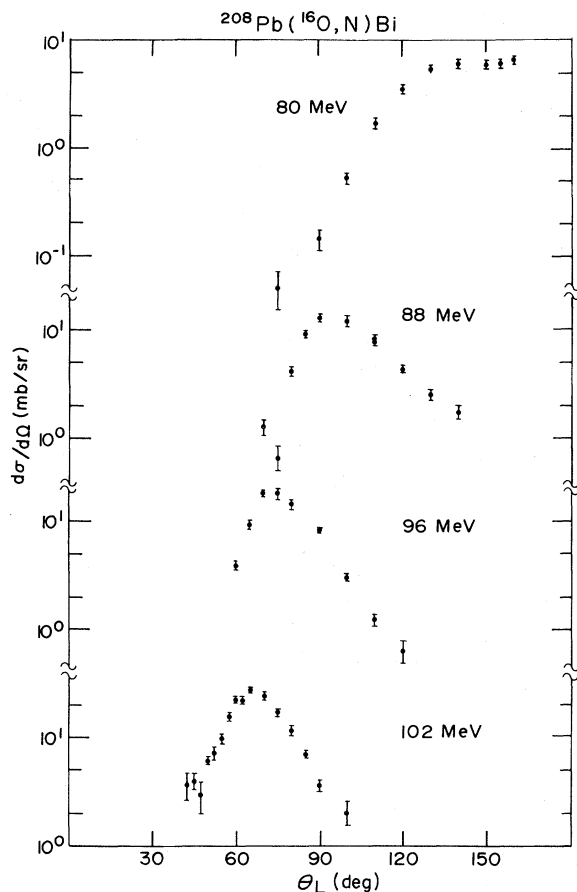


FIG. 7. Angular distributions corresponding to the total energy integrated cross section in the N exit channel for 80, 88, 96, and 102 MeV ^{16}O incident on ^{208}Pb . The progression from a backward peaked angular distribution at 80 MeV incident energy, which is near the entrance channel Coulomb barrier, to a "grazing peak" which moves to smaller angles with increasing incident energy is observed.

method, rather than assuming a $1/\sin\theta$ dependence of the angular distributions, depress the cross sections by about 15% at the lowest energies and are negligible at the highest energies. The excitation function obtained is presented in Fig. 12.

IV. ELASTIC SCATTERING

Considerable $^{16}\text{O} + ^{208}\text{Pb}$ elastic scattering data exist from the present work and from other studies^{4,5} for incident energies between the Coulomb barrier and 104 MeV. The heavy-ion version of the optical-model search codes ABACUS¹⁰ and HIGENOA¹¹ has been used to analyze these data and the $^{16}\text{O} + ^{181}\text{Ta}$ elastic data in a systematic

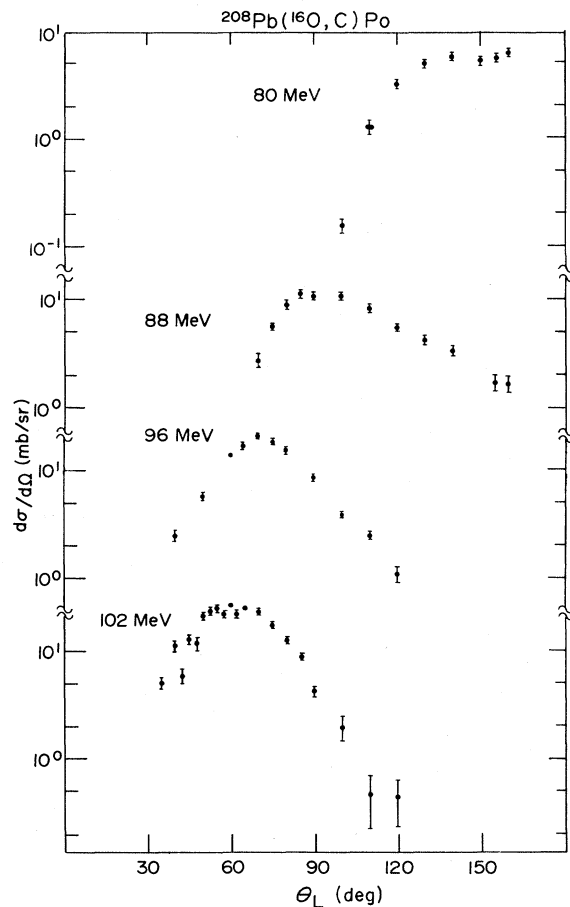


FIG. 8. Angular distributions corresponding to the total energy integrated cross section in the C exit channel for 80, 88, 96, and 102 MeV ^{16}O incident on ^{208}Pb . An energy dependence of the maximum of the angular distribution similar to that observed for the N exit channels (Fig. 7) also is obtained for the C cross sections. Except at the lowest incident energy, however, the C angular distributions are broader and are peaked at a more forward angle than the corresponding $^{208}\text{Pb}(^{16}\text{O}, \text{N})$ angular distribution.

TABLE I. Experimental total cross sections.

Target	E_{lab} (MeV)	$\sigma(O')^a$ (mb)	$\sigma(N)$ (mb)	$\sigma(C)$ (mb)	$\sigma(B)$ (mb)	$\sigma(\text{Fis})$ (mb)	σ_{qe}^b (mb)
^{208}Pb	80	24 ± 4	21 ± 2	19 ± 2		36 ± 4	64 ± 8
	83	60 ± 12	33 ± 2	36 ± 3	0.22 ± 0.1	108 ± 10	129 ± 18
	88	117 ± 25	48 ± 3	57 ± 3	0.80 ± 0.2	350 ± 40	222 ± 31
	90	92 ± 20	48 ± 2	60 ± 3	1.6 ± 0.2	377 ± 50	201 ± 25
	96	c	52 ± 2	73 ± 2	≤ 3.0	685 ± 70	c
	102	157 ± 20	65 ± 3	89 ± 4	1.5 ± 0.7	844 ± 90	313 ± 28
^{181}Ta	83	36 ± 15	44 ± 3	48 ± 3	1.5 ± 1.0	11 ± 1	130 ± 22
	90	37 ± 10	52 ± 2	64 ± 3	3.3 ± 0.6	49 ± 5	156 ± 15
	96	43 ± 10	59 ± 2	76 ± 4	8.9 ± 2.0	140 ± 14	187 ± 16

^a Contains contributions from ^{16}O inelastic plus ^{17}O and ^{18}O transfer channels.

^b Sum of $\sigma(O')$, $\sigma(N)$, $\sigma(C)$, and $\sigma(B)$.

^c Data not sufficient to resolve O quasielastic from elastic.

way. In the analysis, Woods-Saxon potentials with identical real and imaginary geometry were used. In the automatic searches the radius and imaginary well depth were varied for a fixed real potential of $V_0 = 100$ MeV and various diffusivities ($0.45 \leq a \leq 0.55$ fm). The best-fit potentials for $a = 0.45, 0.50,$ and 0.55 fm are tabulated in Table II and the resulting best fits are shown with the Ta and Pb experimental data in Figs. 13 and 14, respectively. Nearly identical total reaction cross sections were predicted for the best-fit parameter sets with different diffusivities.

The grazing angular momentum l_g and the predicted total reaction cross section σ_R obtained from the optical-model calculations¹² are compared in Table III with similar values obtained from a "quarter-point" analysis¹³ of the elastic scattering. The variation in l_g and σ_R for the different optical-model parameter sets which reproduce the elastic scattering data is small as seen from Table II. At the lowest incident energies, which are near the Coulomb barrier, the grazing angular momentum l_g obtained from the optical-model analysis of the Pb data is ~ 4 units larger than the corresponding value from the quarter-point analysis (see Table III). This discrepancy decreases at higher incident energies; however, at the highest energy the value from the optical-model analysis remains nearly one unit larger than that of the quarter-point formula. Such a variation in the grazing angular momentum also is reflected in the total reaction cross sections predicted using these two prescriptions.^{12,13} In both analyses $\sigma_R \sim \pi\lambda^2(l_g + 1)^2$. Indeed the sum of the measured Pb fission and quasielastic cross sections (σ_f and σ_{qe} of Table I) exceeds the quarter-point total reaction cross section by as much as 50% at incident energies near the Coulomb barrier.

Two potentials of Woods-Saxon geometry with constant well depths and varying diffusivities can only have identical values in the exponential region at a single radius. Therefore, the radial region in which the potentials are determined by the elastic scattering data may be studied by fitting the same data with Woods-Saxon potentials of different diffusivity.¹⁴ This is illustrated in Fig. 15 where groups of real nuclear potentials with varying diffusivity, which give a nearly identical description of the 80 and 90 MeV $^{16}\text{O} + ^{208}\text{Pb}$ elastic data, are plotted as a function of the radius. All the potentials shown which fit the 80 and 90 MeV data have nearly identical values at a radius of ~ 12.50 and 12.90 fm, respectively. The figure also illustrates the sensitivity in determining this radius. Similar radii have been determined for the $^{16}\text{O} + ^{208}\text{Pb}$ data at the other incident energies, and this sensitive radius ($\equiv R_s$) is shown in Fig. 16 as a function of the incident energy. Also shown in this figure for comparison are strong-absorption radii as determined¹³ from the angle at which the elastic scattering falls to $\frac{1}{4}$ of the Rutherford cross section, and from the angular momenta for which the transmission coefficient determined from the optical-model analysis equal 0.5. The sensitive radius obtained from fits to the elastic data with varying diffuseness increases with increasing incident energy, up to 90–95 MeV. At high bombarding energies, however, the value of such sensitive radii no longer increase. In fact, above an incident energy of 90 MeV, the radius at which the optical-model parameters are determined is independent of energy within the errors of the analysis (see Fig. 16). A similar analysis of $^{16}\text{O} + ^{208}\text{Pb}$ elastic data at 129.5, 140, 192, and 216.6 MeV measured elsewhere^{5,6} gives values for the optical-model sensitive radius between 12.8 and 13.2 fm. The quarter-point strong-

absorption radii are nearly constant as a function of incident energy and the strong-absorption radii (using Rutherford orbit) determined from $T_i = 0.5$ decrease slightly with increasing incident energy.

It is apparent (see Fig. 16) that for incident energies near the Coulomb barrier there are sizable differences between the radii determined from

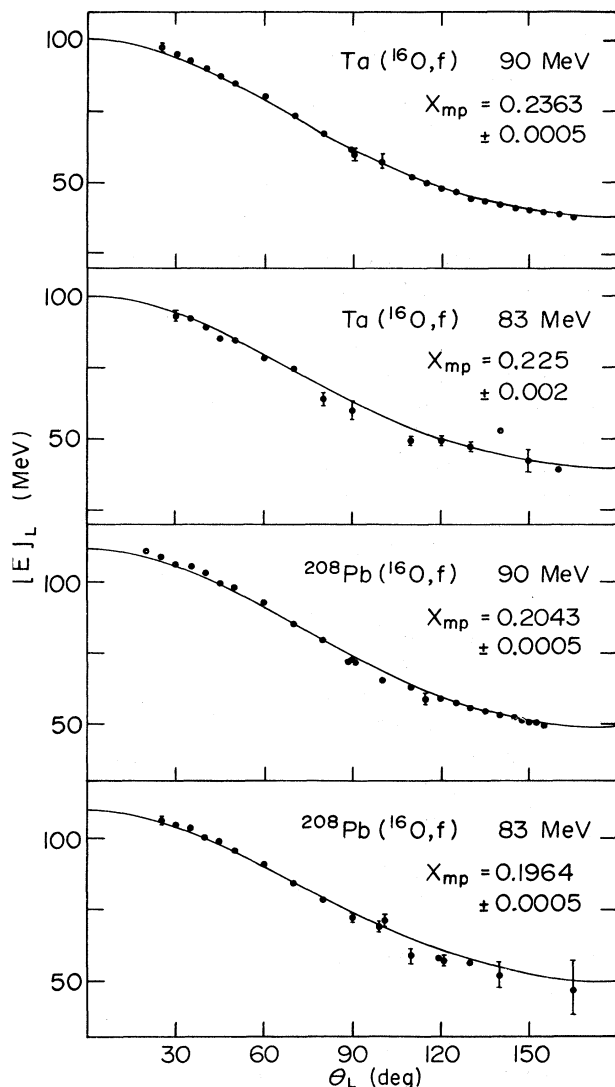


FIG. 9. Mean laboratory kinetic energy of the fission products resulting from 83 and 90 MeV ^{16}O incident on ^{181}Ta and ^{208}Pb plotted versus laboratory angle. The kinetic energies have been corrected for energy loss in the target. The full drawn curves are fits to the data using Eq. (2). The resulting values of χ , also given in the figure, are used as described in Ref. 9 to obtain fission differential cross sections in the center-of-mass system. The errors on χ do not include systematic errors.

fitting the data with potentials of varying diffusivity and those values determined from $T_i = 0.5$ (crosses) and from a quarter-point analysis (open circles). Similar discrepancies recently have been noted¹⁴ in the analysis of 100 MeV ^{32}S elastic scattering on ^{27}Al .

The sharp decrease in R_s as the incident energy approaches the Coulomb barrier from above is not understood. Elastic scattering usually is thought to determine the height and radius of an interaction barrier that is the sum of the potentials associated with the Coulomb and nuclear forces and angular momentum. It is expected that as energy and angular momentum increase such a barrier position will move toward smaller radii.

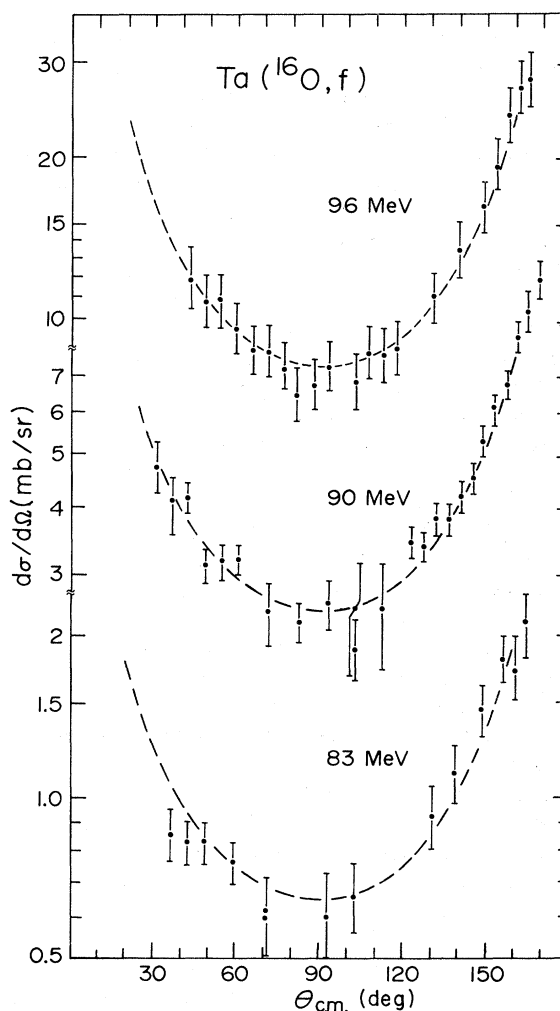


FIG. 10. Fission angular distributions in the center-of-mass system for $^{16}\text{O} + ^{181}\text{Ta}$ at 83, 90, and 96 MeV incident energies. The dashed curves are a $(\sin\theta)^{-1}$ fit to the data.

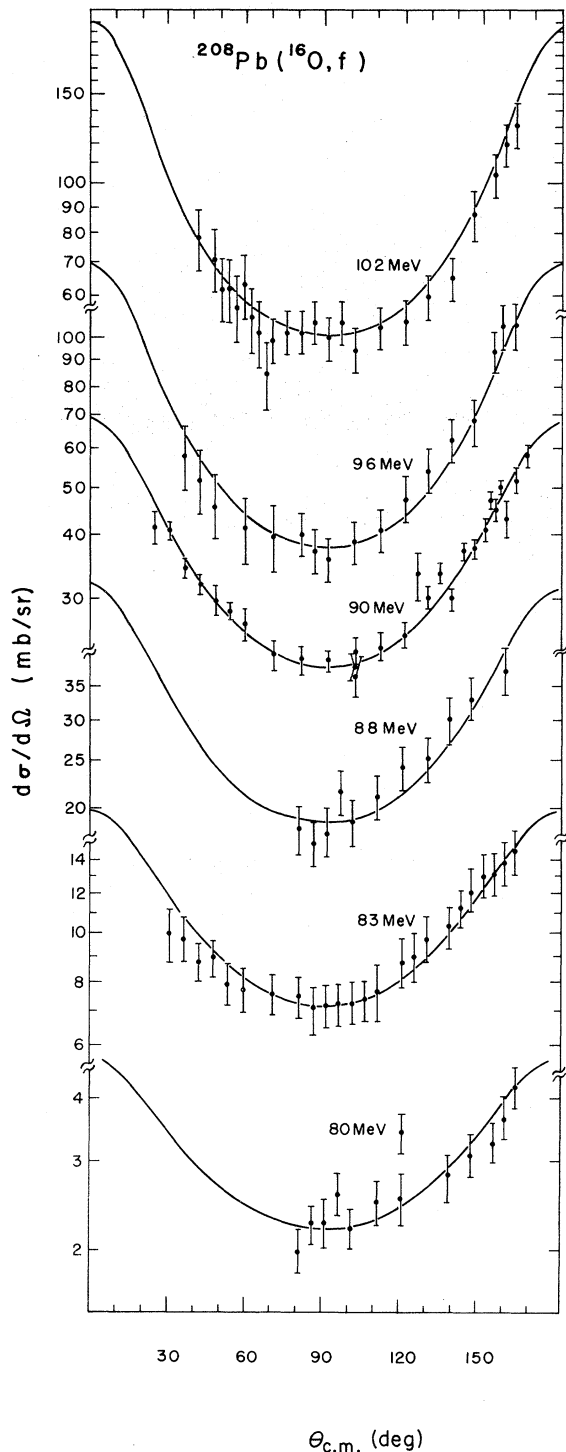


FIG. 11. Fission angular distributions in the center-of-mass system for $^{16}\text{O} + ^{208}\text{Pb}$ at 80, 83, 88, 90, 96, and 102 MeV incident energies. The solid curve is a fit to the data using Eq. (3) and the parameters given in Table V.

V. QUASIELASTIC AND FISSION CROSS SECTIONS

Representative angular distributions for the energy integrated O, N, C, B, and Be cross sections are shown in Figs. 5–8. No events were observed corresponding to ejectiles with $Z \geq 9$. All the angular distributions are typical of a grazing collision; however, differences exist between the various final quasielastic channels. The C and Be distributions, for example, are considerably broader than the distributions for the N and O' channels. The strength for the O' and N channel is concentrated in a few discrete states below 3 MeV of excitation while the strength

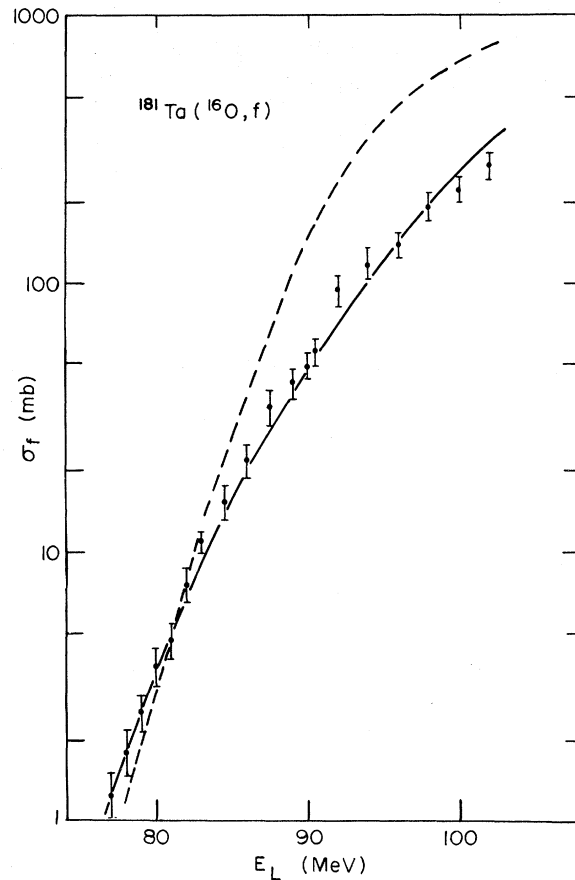


FIG. 12. Total fission cross section for $^{16}\text{O} + ^{181}\text{Ta}$ as a function of the incident laboratory energy. The data at 83, 90, and 96 MeV incident energies were obtained by measuring the angular distribution of fission products, see Fig. 10. The remaining data points were obtained as described in Sec. III of the text from measurements at laboratory angles of 77° and 160° . The full drawn curve is a calculation of the energy dependence of the total fission cross section using the code ALICE (Ref. 7) and an s -wave fission barrier $B_f = 13.8$ MeV. The dashed curve is obtained for a value of $B_f = 18.0$ MeV. See the text for further details of the calculation.

in the C channel is contained in a broad bump of overlapping states centered about a large negative Q value (~ -30 MeV). The carbon groups consist of roughly equal amounts of ^{12}C and ^{14}C . The ^{13}C cross section is more difficult to judge from the present data but at the higher incident energies seems to be comparable with the ^{12}C and ^{14}C cross sections. This feature is in agreement with a study¹⁵ of reactions induced by 137 MeV ^{16}O on ^{197}Au . In that work, however, the angular distributions are forward peaked for the carbon and lighter groups while the nitrogen channel still shows evidence of a grazing peak.

The magnitude of the total cross sections for the C and N channels is similar for both targets

TABLE II. Optical-model parameters:

$$V_N(r) = (V + iW)[1 + \exp(r - R/a)]^{-1},$$

$$\text{where } R = r_0[(16)^{1/3} + (A_{\text{tar}})^{1/3}].$$

E_L (MeV)	V (MeV)	W (MeV)	r_0 (fm)	a (fm)	σ_R^a (mb)	l_g^b (\hbar)
$^{16}\text{O} + ^{208}\text{Pb}$						
80	100	23.4	1.272	0.45	113	9.9
	100	21.8	1.249	0.50	113	9.8
	100	21.8	1.225	0.55	118	9.3
83	100	46.8	1.266	0.45	286	20.5
	100	37.9	1.244	0.50	287	20.3
88	100	41.8	1.215	0.55	292	20.0
	100	65.4	1.260	0.45	556	30.6
	100	64.6	1.232	0.50	562	30.4
90	100	67.4	1.202	0.55	570	30.3
	100	66.4	1.262	0.45	664	34.0
	100	66.9	1.233	0.50	668	33.8
94 ^c	100	73.6	1.203	0.55	686	33.9
	100	71.9	1.263	0.45	861	39.8
	100	81.8	1.232	0.50	876	39.9
96	100	84.6	1.201	0.55	884	39.8
	100	54.7	1.266	0.45	928	41.9
	100	66.5	1.234	0.50	939	41.9
102	100	82.4	1.204	0.55	977	42.5
	100	57.3	1.261	0.45	1147	48.2
	100	71.4	1.227	0.50	1156	48.1
100	65.5	1.202	0.55	1161	48.0	
$^{16}\text{O} + ^{181}\text{Ta}$						
83	100	125.9	1.226	0.45	577	29.9
	100	123.5	1.191	0.50	575	29.6
	100	141.0	1.156	0.55	602	30.0
90	100	99.7	1.230	0.45	879	38.9
	100	114.7	1.195	0.50	894	39.0
	100	125.0	1.160	0.55	911	39.2
96	100	85.8	1.246	0.45	1155	46.4
	100	97.4	1.212	0.50	1168	46.4
	100	104.6	1.179	0.55	1180	46.4

^aTotal reaction cross section calculated from the optical model— see Ref. 12.

^bGrazing angular momentum— see Ref. 12.

^cData from Ref. 4.

and at all the incident energies studied. For the ^{181}Ta target nucleus the integrated cross section for the neutron transfer is about the same and has a similar energy dependence as for the single-proton transfer. This is in contrast to the ^{208}Pb results, where the integrated cross section for the ^{17}O quasielastic channel is much larger than for the other transfer channels. The few-nucleon-transfer cross section increases fairly rapidly for the incident energies just above the Coulomb barrier; however, the rate of increase is somewhat reduced at higher energies (see Fig. 17). The cross sections corresponding to the B and Be channels are much smaller than for the other observed final products (see Table I). For the ^{208}Pb target such data are too sporadic for a systematic trend to be distinguished in the present data. However, in the Ta data, where the incident

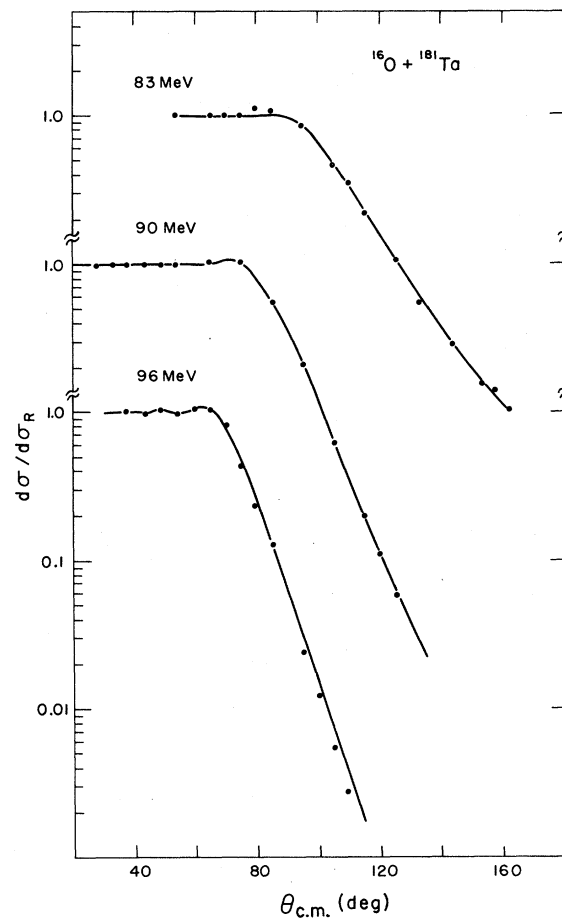


FIG. 13. Angular distributions of ^{16}O elastically scattered from ^{181}Ta plotted as a ratio to the Rutherford cross section. The full drawn curves are optical-model calculations based on the parameters ($a = 0.50$ fm) given in Table II.

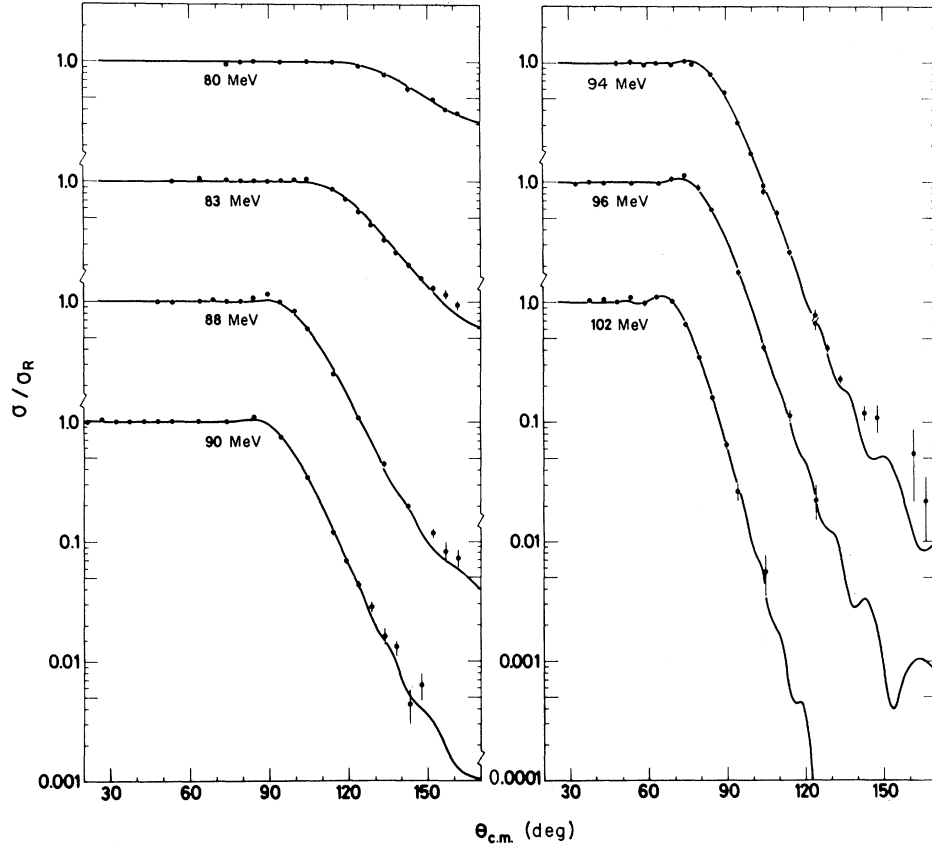


FIG. 14. Angular distributions of the ^{16}O elastically scattered from ^{208}Pb at 80, 83, 88, 90, 94, 96, and 102 MeV. The data for 94 MeV are from Ref. 4. The full drawn curves are optical-model calculations based on the parameters (with $a = 0.50$ fm) given in Table II. Nearly identical cross sections are obtained for the other corresponding parameter sets given in Table II.

TABLE III. Comparison of grazing angular momentum and total reaction cross sections calculated from the optical model and from the quarter point of the elastic data.

Target	E_L (MeV)	$E_{c.m.}$ (MeV)	quarter point ^a			optical model ^b		
			$\theta_{1/4}$ (deg)	l_g (\hbar)	σ_R (mb)	l_g (\hbar)	σ_R (mb)	$\sigma_R(\text{o.m.})/\sigma_R(\text{q.p.})^c$
^{208}Pb	80	74.29	d	d	d	9.8	113	d
	83	77.07	139	16.5	174	20.3	287	1.65
	88	81.71	115	27.5	440	30.4	562	1.28
	90	83.57	107	31.7	565	33.8	668	1.18
	94	87.29	96	37.9	763	39.9	876	1.15
	96	89.14	92	40.2	840	41.9	939	1.12
	102	94.71	82	46.5	1053	48.1	1156	1.10
^{181}Ta	104	96.57	78	49.5	1166	50.9	1268	1.09
	83	76.26	114	25.6	419	29.6	571	1.36
	90	82.69	93	36.2	753	39.0	894	1.19
	96	88.20	80	44.1	1039	46.4	1168	1.12

^a Values from the quarter-point analysis as defined in Ref. 13.

^b Values from optical-model calculations as defined in Ref. 12. These values were obtained using the optical-model parameter set from Table II with $a = 0.50$ fm.

^c Ratio of total reaction cross section obtained in optical-model and quarter-point analyses.

^d Elastic data do not fall to a quarter of the Rutherford value; therefore quarter-point analysis is not defined.

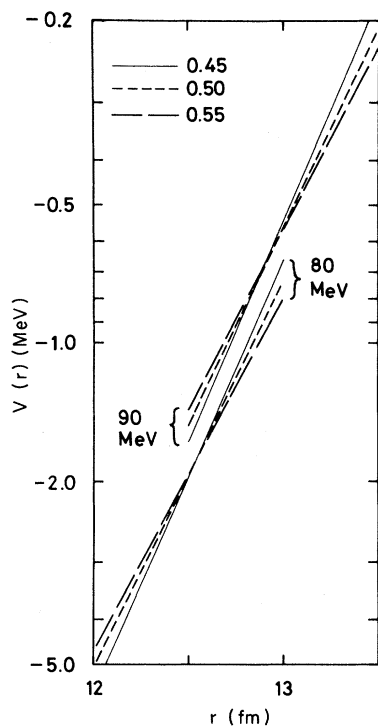


FIG. 15. Log plot of the "best fit" real nuclear potentials for 80 and 90 MeV $^{16}\text{O} + ^{208}\text{Pb}$ as a function of the channel radius. The potentials indicated by the solid short dashed and long dashed lines correspond to best fit potentials with diffusivities of 0.45, 0.50, and 0.55 fm, respectively; see Table II for the optical-model parameters. The potentials for the same energy are nearly identical in magnitude at a radius of ~ 12.5 and 12.9 fm for the 80 and 90 MeV data, respectively.

energies are well above the Coulomb barrier, the cross section for a boron ejectile increases rapidly with increasing energy (see Fig. 18).

The total quasielastic cross section, i.e., the sum of the cross section for inelastic and few-nucleon transfer, makes up a sizable fraction of the total reaction cross section of ^{16}O on both ^{181}Ta and ^{208}Pb targets. Ratios of $\sigma_{qe}/\sigma_R \geq 0.5$ are observed for $^{16}\text{O} + ^{208}\text{Pb}$ near the Coulomb barrier (see Table IV). This ratio decreases to ~ 0.25 at the highest energy measured for the ^{208}Pb target. For the ^{181}Ta target the measured quasielastic cross section accounts for a smaller fraction of the total-reaction cross section (see Table IV). The difference between the Ta and Pb quasielastic cross sections appears to be in the O channels (see Table I). The inelastic excitation to the low-lying states in ^{181}Ta , which were not resolved from the elastic group, could well be significant and large enough to account for the observed difference. These ratios of quasielastic to total

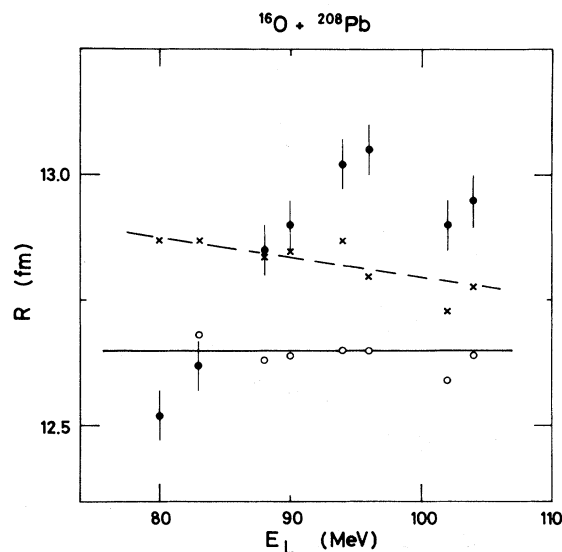


FIG. 16. Optical-model sensitive radius, solid points (at which optical-model real potentials determined from fitting ^{16}O plus ^{208}Pb elastic scattering with varying diffusivities have nearly identical values—see text and Fig. 15) shown as a function of incident energy. Also shown for comparison are strong absorption radii as determined from the angle at which the elastic scattering falls to $\frac{1}{4}$ of the Rutherford cross section (open circles), and from the angular momenta for which the transmission coefficient determined from the optical-model analysis equals $\frac{1}{2}$ (crosses). The solid and broken lines indicate the trend of the strong absorption radii.

cross sections obtained in the present work are not consistent with the ratios of the compound-nuclear and total reaction cross sections which appear in the literature. For example, Sikkeland¹⁶ concludes, from a rather limited set of data, that $\sigma_{CN} \sim 0.72 \sigma_R$ for ^{16}O induced reactions independent of target and incident energy.

The total fission cross sections σ_f also are shown as a function of the incident ^{16}O energy for the ^{181}Ta and ^{208}Pb targets in Figs. 17 and 18, respectively. The fission almost certainly results from the compound system (first chance fission) or from a nucleus in the decay chain of the compound system (second, third, etc., chance fission). The quasielastic processes that have large cross sections leave residual nuclei at excitation energies below (or perhaps in the C channels near) the fission barrier, which is much higher than the particle emission thresholds for nuclei¹⁷⁻¹⁹ near $A = 181$ and 208 . Cross sections for ^{16}O induced reactions, e.g., $(^{16}\text{O}, \alpha)$ transfer, on heavy targets, in which most of the mass of the projectile is transferred to the target are expected to be extremely small.²⁰

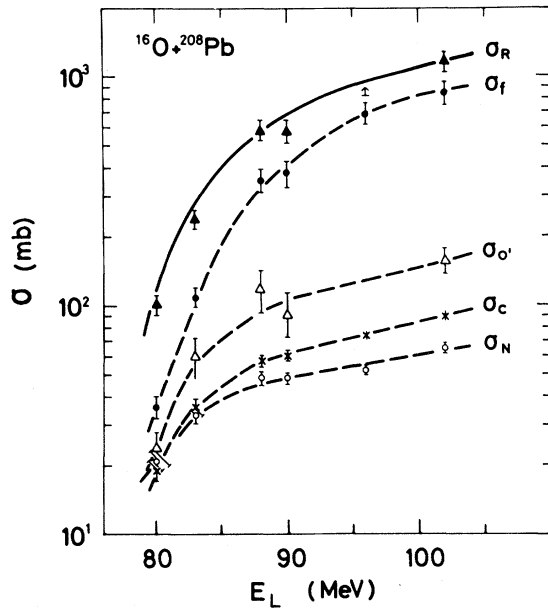


FIG. 17. Total cross sections measured for the various quasielastic processes and fission induced by ^{16}O on ^{208}Pb as a function of the incident energy. σ_f , $\sigma_{O'}$, σ_N , and σ_C are designated by solid circles, open triangles, open circles, and crosses, respectively. The 82 and 94 MeV quasielastic cross sections are from Ref. 4. The experimental quasielastic and fission cross sections shown are summarized in Table I. The curves shown with the quasielastic and fission cross sections are only to guide the eye. Also shown is a comparison between the total cross sections measured in the quasielastic plus fission channels (solid triangles) and the reaction cross section, σ_R , predicted from the optical model—see Table II.

The sum of the measured quasielastic and fission cross sections for ^{16}O on ^{208}Pb is compared in Table IV with the total-reaction cross section obtained from the optical-model calculation using parameters which reproduce the elastic scattering data. Within the uncertainties of the measurements, these reaction channels account for nearly all of the reaction cross section as determined from the optical model. Thus the probability of fission in the deexcitation of the compound system ^{224}Th formed from $^{16}\text{O} + ^{208}\text{Pb}$ must be large. This is not surprising, since the s -wave fission barrier of the lightest measured Th nuclei is 6–7 MeV,²¹ which is of the order of the particle emission threshold for these systems ($B_n = 7.73$, 6.02, and 7.80 MeV for ^{224}Th , ^{233}Th , and ^{222}Th , respectively²²). Furthermore, there is sufficient excitation energy available in the compound system (see Table IV) for fission to compete after emission of one or more particles. Measured compound-evaporation-residue cross sections²³ for

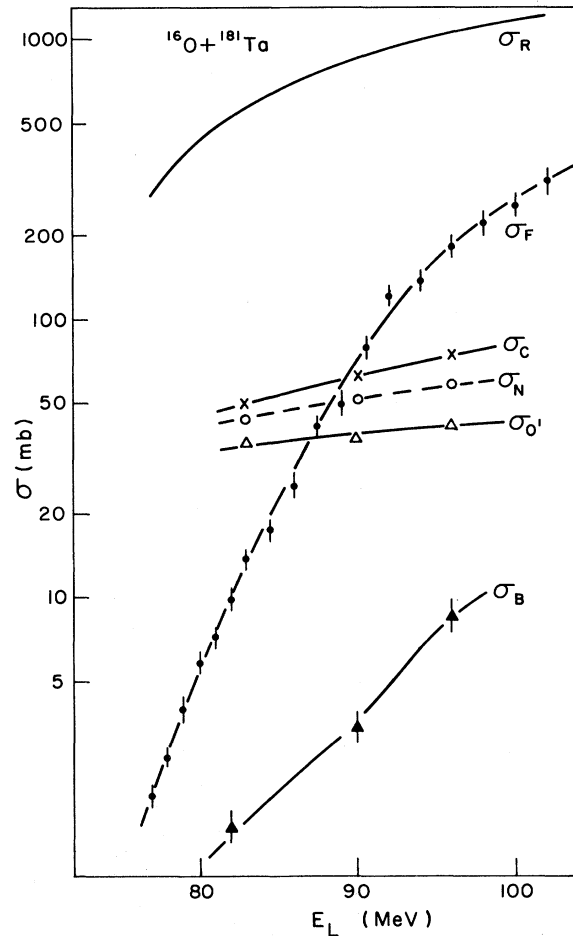


FIG. 18. Total cross sections measured for the various quasielastic processes and fission induced by ^{16}O on ^{181}Ta as a function of the incident energy. σ_f , $\sigma_{O'}$, σ_N , σ_C , and σ_B are designated by solid circles, open triangles, open circles, crosses, and closed triangles, respectively. The curves shown with the quasielastic and fission data are only to guide the eye. The oxygen quasielastic channel does not include inelastic ^{16}O processes populating states in ^{181}Ta below an excitation of 1.5 MeV. The 83, 90, and 96 MeV cross sections are summarized in Table I. The remaining fission cross sections are described in the text and in the caption to Fig. 12. Also shown is the total reaction cross section σ_R predicted from the optical model.

83–91 MeV $^{16}\text{O} + ^{206}\text{Pb}$ are of the order of a few mb, which is much less than the uncertainties in our measured cross sections.

In contrast, for $^{16}\text{O} + ^{181}\text{Ta}$, the fission and quasielastic channels only account for a small fraction of the total reaction cross section, as obtained from the optical model (see Fig. 18). Presumably, this is the result of a fission barrier in the ^{197}Tl compound and lighter Tl systems that is much higher than the particle emission thresh-

holds. Indeed measured fission barriers¹⁷⁻¹⁹ in this mass region are ~ 22 MeV compared with neutron binding energies²² of 8.98, 7.55, and 9.36 for ¹⁹⁷Tl, ¹⁹⁶Tl, and ¹⁹⁵Tl, respectively. Therefore, the evaporation-residue cross section should account for a large part of the total reaction cross section of ¹⁶O + ¹⁸¹Ta.

VI. FISSION ANGULAR DISTRIBUTIONS

The angular distributions for fission fragments are presented in Figs. 10 and 11. In the case of the Ta target the distributions are compared with the $(\sin\theta)^{-1}$ dependence predicted for the decay of high-angular-momentum states. The differences between the experimental results and these distributions are small and no further attempts to analyze this prediction were made. The angular dependence of the ²⁰⁸Pb data, however, deviates considerably from $(\sin\theta)^{-1}$ and, therefore, is discussed in further detail.

The fission fragment angular distribution can be expressed as¹⁸

$$W(\theta) = \sum_l (2l+1)^2 T_l' \frac{\exp(-x) J_0(ix)}{\text{erf}[(l + \frac{1}{2})/(2K_0^2)^{1/2}]}. \quad (3)$$

Here J_0 is the zero-order Bessel function, K_0^2 is the width of the spin distribution of K states at the saddle point, T_l' is the transmission coefficient for the initial spin distribution of the compound system, and x is given by the expression

$$x = (l + \frac{1}{2})^2 (\sin^2 \theta) / 4K_0^2. \quad (4)$$

This expression is valid for first-chance fission of systems formed with spinless particles where the initial population of M substates is restricted to $M=0$. For the case of ¹⁶O + ²⁰⁸Pb, where fission after particle emission can contribute, this expression was used, assuming that the prefission neutron emission does not significantly alter the initial spins and magnetic-substate distributions. Thus K_0^2 is interpreted as an average width of the spin distribution for the various products which contribute to fission. The transmission coefficient T' corresponding to the fissioning system is parametrized as^{24, 25}

$$T_l' = 1 - \{1 + \exp[(l_c - l)/\Delta]\}^{-2}. \quad (5)$$

Values of l_c and Δ are used which reproduce the measured fission cross section σ_f (see Table I), i.e.,

$$\sigma_f = \pi \lambda^2 \sum_l (2l+1) T_l'. \quad (6)$$

The values of l_c and Δ used to define the spin distributions of the compound system are given in Table V. The transmission coefficients and partial cross sections [$\sigma_l = \pi \lambda^2 (2l+1) T_l'$] corresponding to the optical-model analysis and the assumed parametrization of the spin distribution of the compound fissioning system are shown in Fig. 19 for the case of 90 MeV ¹⁶O + ²⁰⁸Pb. Such a description of the spin distribution for the compound system is arbitrary. It is felt, however, that it is more physical than a sharp cutoff in l space, especially for the present study where the incident energies are near the Coulomb barrier.

Angular distributions of the ¹⁶O + ²⁰⁸Pb fission fragments fitted by varying K_0 are shown with the experimental distributions in Fig. 11. The corresponding best-fit values of K_0 are given in Table V together with an uncertainty determined from the data analysis. A trend of increasing K_0 with increasing bombarding energy is perhaps present. It is emphasized, however, that the observed changes of the angular shapes with energy are determined primarily by the initial spin distributions and to a lesser extent by changes of K_0 .

The width of the spin distribution of K states at

TABLE IV. Comparison of measured quasielastic and fission cross sections calculated from the optical model.

Target	E_L (MeV)	E_{CN}^* (MeV) ^a	σ_{qe}/σ_R ^b	$(\sigma_{qe} + \sigma_f)/\sigma_R$ ^c	l_{sc} ^d
²⁰⁸ Pb	80	27.80	0.57 ± 0.07	0.88 ± 0.11	11.2
	82 ^e	29.65	0.43	e	16.1
	83	30.58	0.45 ± 0.06	0.83 ± 0.10	17.2
	88	35.22	0.40 ± 0.06	1.02 ± 0.13	24.7
	90	37.08	0.30 ± 0.04	0.87 ± 0.11	29.4
	94 ^e	40.80	0.38	e	32.0
	96	42.65	$>0.13^f$	$>0.86^f$	
¹⁸¹ Ta	102	48.22	0.27 ± 0.02	0.99 ± 0.10	41.7
	83	51.46	0.23 ± 0.04	0.25 ± 0.04	28.7
	90	57.89	0.18 ± 0.02	0.23 ± 0.02	37.5
	96	63.40	0.16 ± 0.01	0.28 ± 0.03	44.0

^aExcitation energy in the compound systems ²²⁴Th (²⁰⁸Pb target) and ¹⁹⁷Tl (¹⁸¹Ta target).

^bRatio of measured quasielastic cross section to total reaction cross section (see Table I) as calculated from the optical model using parameters given in Table II ($\alpha=0.50$).

^cRatio of measured quasielastic plus fission cross section (Table I) to the total reaction cross section.

^dCritical angular momentum corresponding to a sharp division in l of the reaction cross section (as calculated from the optical model) between quasielastic and other processes.

^eData from Ref. 4. Fission cross sections have not been measured.

^fThese values given as lower limits for the 96 MeV data do not include the oxygen quasielastic channels which were not well resolved from the elastic scattering at this energy.

TABLE V. Fission angular distribution parameters for $^{16}\text{O} + ^{208}\text{Pb}$.

E_L (MeV)	E_{CN}^* ^a (MeV)	l_c^b (\hbar)	Δ^b (\hbar)	K_0^c	$\frac{J_{\text{eff}}^d}{\hbar^2 a_f}$
80	27.8	-4.0 ^e	6.0	6 ± 2	$7.8^{+6.0}_{-4.3}$
83	30.6	7.0	5.0	6 ± 2	$7.3^{+5.7}_{-4.1}$
88	35.2	19.5	4.4	7 ± 2	$9.1^{+6.0}_{-4.4}$
90	37.1	21.6	4.0	7 ± 1.5	$8.8^{+4.2}_{-3.4}$
96	42.6	32.2	4.0	8 ± 2	$10.6^{+6.0}_{-4.6}$
102	48.2	37.5	4.0	8 ± 2	$9.9^{+5.5}_{-4.3}$

^aExcitational energy of the ^{224}Th compound system.

^bAssumed values in the parametrization of the transmission coefficients T_l' , of the fissioning system—see Eq. (5) and text.

^cObtained from fitting fission fragment angular distributions—see Fig. 11.

^dObtained from Eq. (9) assuming a value of 6.3 MeV for the fission barrier height.

^eA negative value results if T_l' does not exceed 0.5.

the saddle point K_0 can be related¹⁸ to the nuclear temperature at the saddle point, t , and the effective moment-of-inertia, J_{eff} ,

$$K_0^2 = t J_{\text{eff}} / \hbar^2. \quad (7)$$

An energy-temperature relation²⁶

$$E_x - B_f = a_f t^2 - t \sim a_f t^2 \quad (8)$$

is assumed, where $E_x - B_f$ is the excitation energy of the fissioning system above the fission barrier and a_f is the level-density parameter for the fission states. The ratios

$$\frac{K_0^2}{(E_x - B_f)^{1/2}} = \frac{J_{\text{eff}}}{\hbar^2 a_f^{1/2}} \quad (9)$$

corresponding to the K_0 which was obtained from the analysis of the fission-fragment angular distribution are given in Table V. A value of $B_f = 6.3$ MeV, obtained from the extrapolation of the fission barrier height for heavier Th isotopes,²¹ was assumed as the fission barrier height. Since the determination of K_0 is not precise and $J_{\text{eff}} \sim K_0^2$, the limits for determining an effective moment of inertia are large and are relatively insensitive to either a_f or B_f . Assuming an $a_f = A/8 = 28$ MeV⁻¹, an effective moment of inertia $0.45^{+0.3}_{-0.2}$ times the rigid spherical body values, J_0 , is obtained. Such values are not inconsistent with the liquid-drop prediction²⁷ of $J_{\text{eff}}/J_0 = 0.64$.

VII. FISSION EXCITATION FUNCTIONS

As discussed in Sec. V, fission has a very different role in the deexcitation of the ^{197}Tl and

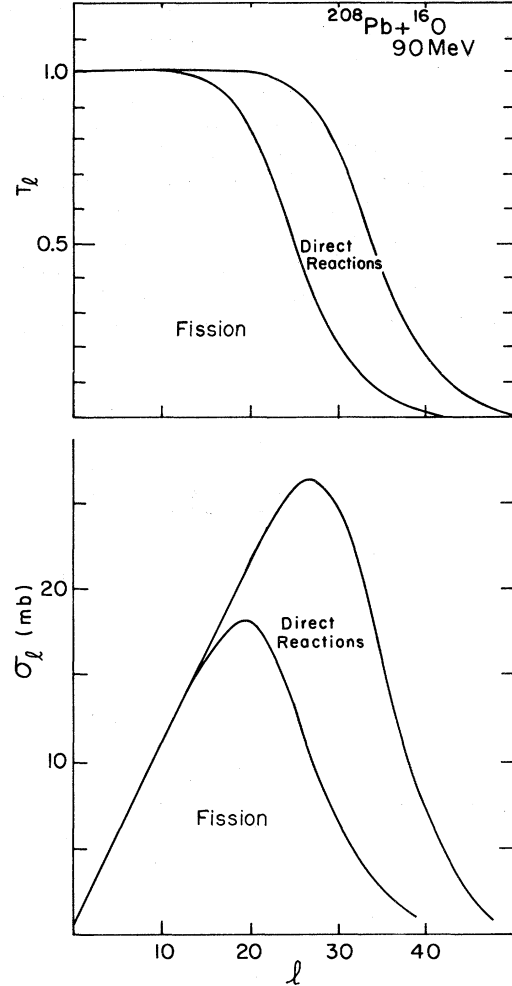


FIG. 19. Optical-model transmission coefficients T_l and partial cross sections $\sigma_l = \pi \lambda^2 (2l + 1) T_l$ are shown as a function of l for 90 MeV ^{16}O incident on ^{208}Pb . Also shown are the transmission coefficients [see Eq. (5) and Table V] and corresponding partial cross sections assumed for the fissioning system in the analysis of the fission angular distributions—see Sec. VI of the text.

^{224}Th compound systems. In the former case the s -wave fission barrier is very much above the particle emission threshold; whereas in the case of ^{224}Th the s -wave fission barrier is similar with the particle emission thresholds. Therefore, fission competes much less favorably in the deexcitation of the ^{197}Tl compound system than in ^{224}Th , even though the compound-nuclear excitation energies for ^{197}Tl are higher than for ^{224}Th (see Table IV).

The increase in the fission cross section for $^{16}\text{O} + ^{181}\text{Ta}$ from a few percent of the total reaction cross section to $\sim 15\%$ of σ_R in the energy range of the excitation-function data can be attributed to

the lowering of the fission barrier with increasing angular momentum. This effect has previously been described⁷ in terms of a rotating liquid drop.²⁸ The code ALICE⁷ has been used to calculate the competition between particle evaporation and fission through the angular-momentum-dependent, rotating liquid-drop fission barrier. The initial spin distribution was calculated from the transmission coefficients obtained from the parabolic approximation²⁹ to a real Woods-Saxon plus Coulomb potential. The parameters of the Woods-Saxon potential were adjusted to reproduce

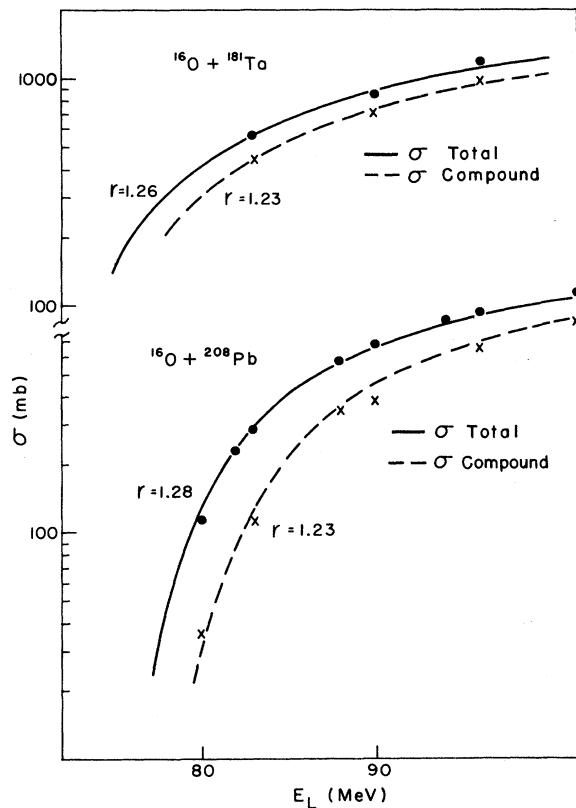


FIG. 20. Comparison of optical-model total reaction cross sections, dots, with reaction cross sections predicted using the parabolic approximation (see Ref. 7) to the sum of the Coulomb and nuclear (Woods-Saxon form with $V = 67$ MeV and $a = 0.57$ fm) potentials. Also shown as crosses is a similar comparison for the total $^{16}\text{O} + ^{208}\text{Pb}$ fission cross section and the difference between the $^{16}\text{O} + ^{208}\text{Pb}$ optical-model total reaction cross section and the measured $^{16}\text{O} + ^{181}\text{Ta}$ quasielastic cross section, $\sigma_R - \sigma_{qe}$. Such cross sections are labeled as compound in the figure. It is possible to reproduce the energy dependence of the total reaction cross sections with radius parameters of 1.26 and 1.29 fm for ^{181}Ta and ^{208}Pb , respectively. The energy dependence of the "compound" cross section for both nuclei can be reproduced with a radius parameter of 1.23 fm.

the energy dependence of the deduced compound cross section—see Fig. 20.

In the ALICE calculation the angular momentum of the composite system was reduced two units for each neutron emitted, three units for proton emission, and 10 units for α -particle emission as prescribed in Ref. 7. To check this assumption the competition between the various particle decays also has been calculated using the statistical deexcitation code³⁰ GROGI. In this calculation angular momentum is conserved at each stage in the particle decay sequence. For the present system, where the Coulomb barriers for charged-particle emission are high, such calculations predict (in agreement with the ALICE calculations) that proton and α -particle emission should be small for the whole range of angular momenta considered. Furthermore, the GROGI calculations indicate that the angular momentum reduction of two units per neutron decay is reasonable.

Predicted $^{16}\text{O} + ^{181}\text{Ta}$ fission excitation functions are shown with the data in Fig. 12. The calculation which reproduces the data was obtained using the liquid-drop value for the s -wave fission barrier ($B_L^f = 13.8$ MeV) and $a_f = 0.97a_n$. (a_f and a_n are the level-density parameters for fission and neutrons, respectively.) Analysis of the previous measurements¹⁷⁻¹⁹ of Γ_f/Γ_n for this mass region from proton and α -particle induced reactions have yielded values of $B_f = 19-23$ MeV and $a_f = (1.10-1.35)a_n$. Such values of B_f are in agreement with recent predictions.³¹ It has not been possible to reproduce the ^{181}Ta ($^{16}\text{O}, f$) excitation function over the entire range of incident energies with such large values of B_f . A calculation of σ_f as a function of the incident energy using a value of $B_f = 1.3 B_L^f = 18.0$ MeV, and $a_f = 1.20a_n$ is shown as the dashed curve in Fig. 12. Variations of a_f/a_n change the magnitude of σ_f ; however, it has not been possible to find an energy independent value of a_f/a_n to reproduce the present excitation function over the entire range of incident energies.

VIII. SUMMARY

Systematic data on elastic, quasielastic, and fission cross sections yield a consistent description of ^{16}O induced reactions near the Coulomb barrier. For $^{16}\text{O} + ^{208}\text{Pb}$, where the s -wave fission barrier for the compound system is comparable with the neutron threshold, nearly the entire total reaction cross section predicted by the optical model is observed in the fission and quasielastic channels. The quasielastic cross section accounts for about half of the total reaction cross section at the Coulomb barrier and still as much as 25%

at the highest incident energies. The observed deviations from a $1/\sin\theta$ dependence for the $^{16}\text{O} + ^{208}\text{Pb}$ fission angular distributions can be accounted for by assuming that the initial spin distribution of the fissioning system is given by the lower (interior) partial waves. The widths of the spin distribution at the saddle point, which reproduce the observed shapes of the fission fragment angular distributions, give a crude estimate of the effective moment of inertia at the saddle point that is not inconsistent with a liquid-drop-model prediction.²⁷

In contrast, the *s*-wave fission barrier is considerably above the particle emission threshold for the compound and daughter Tl system formed by $^{16}\text{O} + ^{181}\text{Ta}$. Thus, a much smaller fission cross section is observed than for $^{16}\text{O} + ^{208}\text{Pb}$. The energy dependence of the $^{16}\text{O} + ^{181}\text{Ta}$ fission cross sections can be reproduced in terms of a rotating liquid-drop model^{7, 28} which yields reduced fission barriers for the higher partial waves. However, to reproduce the $^{16}\text{O} + ^{181}\text{Ta}$ fission excitation function, it is necessary to assume lower values

for the *s*-wave fission barrier (\sim the liquid-drop barrier) than obtained from a similar analysis of light-ion induced fission data.¹⁷⁻¹⁹ The observed $(\sin\theta)^{-1}$ angular distributions for $^{16}\text{O} + ^{181}\text{Ta}$ induced fission is consistent with the assumption that this system undergoes fission from high-angular-momentum states.

An optical-model analysis of the elastic scattering cross sections indicates that these data determine a real nuclear potential in a radial region which increases as the incident energy is raised above the Coulomb barrier. Such an energy dependence was not expected.

Finally, for incident energies near the Coulomb barrier, a significant difference was observed between the optical-model total reaction cross section calculated using potentials which reproduce elastic scattering and such a cross section obtained from the semiclassical quarter-point prescription. The present experimental quasi-elastic and fission cross sections show that for heavy ions such as ^{16}O the quarter-point method should *not* be used near the Coulomb barrier.

*Permanent address: The Niels Bohr Institute, University of Copenhagen, Copenhagen, Denmark.

†This work performed under the auspices of E.R.D.A.

¹R. L. Kozub, N. H. Lu, J. M. Miller, D. Logen, T. W. Debiak, and L. Kowalski, *Phys. Rev. C* **11**, 1497 (1975).

²J. B. Natowitz, E. T. Chulick, and M. N. Namboodiri, *Phys. Rev. C* **6**, 2133 (1972).

³R. Broda, M. Ishihara, B. Herskind, H. Oeschler, S. Ogaza, and R. Ryde, *Nucl. Phys. A* **248**, 356 (1975).

⁴W. von Oertzen, C. E. Thorn, A. Z. Schwarzschild, and J. D. Garrett, in *Proceedings of the International Conference on Reactions between Complex Nuclei, Nashville, June 1974*, edited by R. L. Robinson, F. K. McGowan, J. B. Ball, and J. H. Hamilton (North-Holland, Amsterdam, 1974), Vol. I, p. 83; *Bull. Am. Phys. Soc.* **19**, 1025 (1974); and (unpublished). See also J. D. Garrett, in *Proceedings of the Symposium on Classical and Quantum Mechanical Aspects of Heavy Ion Collisions, Heidelberg, October 1974*, edited by J. L. Harney, P. Braun-Munzinger, and C. K. Gelbke (Springer, Berlin, 1975), p. 59.

⁵D. G. Kovar, B. G. Harvey, F. D. Becchetti, J. Mahoney, D. L. Hendrie, J. Homeyer, W. von Oertzen, and M. A. Nagarajan, *Phys. Rev. Lett.* **30**, 1075 (1973).

⁶J. B. Ball, C. B. Fulmer, E. E. Gross, M. L. Halbert, D. C. Hensley, C. A. Ludemann, M. J. Saltmarsh, and G. R. Satchler, *Nucl. Phys. A* **252**, 208 (1975).

⁷F. Plasil and M. Blann, *Phys. Rev. C* **11**, 508 (1975).

⁸H. Schmidt, W. Kiker, and C. Williams, *Phys. Rev.* **137**, B837 (1965).

⁹T. Sikkeland, A. E. Larsh, and G. E. Gordon, *Phys. Rev.* **123**, 2112 (1961).

¹⁰E. H. Auerbach (unpublished).

¹¹F. G. Perey, L. W. Owen, S. D. Blazier, and C. Y. Wong (unpublished).

¹²The usual definitions of l_g as the angular momentum for which the transmission coefficient $T_l \equiv 1 - |\eta_l|^2 = \frac{1}{2}$ and $\sigma_R = \pi\lambda^2 \sum_{l=1}^{\infty} (2l+1)T_l$ are used. Here η_l is the partial wave scattering amplitude as defined, e.g., by G. R. Satchler in *Proceedings of the International Conference on Reactions between Complex Nuclei, Nashville, June 1974* (see Ref. 4), Vol. II, p. 171.

¹³In the quarter-point analysis a grazing angular momentum is defined as $l_g + \frac{1}{2} = \eta \cot \frac{1}{2} \theta_{1/4}$ where $\eta = Z_1 Z_2 e^2 / \hbar v$ is the Coulomb parameter and $\theta_{1/4}$ is the center-of-mass angle at which the experimental differential cross section falls to $\frac{1}{4}$ of the Rutherford value. A predicted total reaction cross section then can be obtained from $\sigma_R = \pi\lambda^2 (l_g + 1)^2$, and a strong absorption radius can be defined as the distance of closest approach for a Rutherford orbit given by $kR = \eta(1 + \csc \frac{1}{2} \theta_{1/4})$. For a more complete discussion of the quarter-point analysis, see, e.g., J. S. Blair, *Phys. Rev.* **95**, 1218 (1954) and W. E. Frahn, *Ann. Phys. (N.Y.)* **72**, 524 (1972).

¹⁴J. D. Garrett, H. E. Wegner, T. M. Cormier, E. R. Cosman, O. Hansen, and A. J. Lazzarini, *Phys. Rev. C* **12**, 489 (1975).

¹⁵Y. Eyal, K. Beg, D. Logan, F. Miller, and A. Zebelmann, *Phys. Rev. C* **8**, 1109 (1973).

¹⁶T. Sikkeland, *Phys. Rev.* **135**, B669 (1964).

¹⁷D. S. Burnett, R. C. Gatti, F. Plasil, P. B. Price, W. J. Swiatecki, and S. G. Thompson, *Phys. Rev.* **134**, B952 (1964).

¹⁸R. Vandenbosch and J. Huizenga, *Nuclear Fission* (Academic, New York, 1973).

- ¹⁹A. Khodai-Joopari, Univ. of California Radiation Laboratory, Berkeley, Report No. CRL-16489, 1966 (unpublished), and as quoted in Ref. 20.
- ²⁰H. E. Wegner, P. Thieberger, and J. D. Garrett, in *Proceedings of the International Conference on Reactions between Complex Nuclei, Nashville, June 1974* (see Ref. 4), Vol. I, p. 85.
- ²¹B. B. Back, H. C. Britt, O. Hansen, B. Leroux, and J. D. Garrett, *Phys. Rev. C* **10**, 1948 (1974); B. B. Back, O. Hansen, H. C. Britt, and J. D. Garrett, *Phys. Rev. C* **9**, 1924 (1974).
- ²²A. H. Wapstra and N. B. Gove, *Nucl. Data* **A9**, 265 (1971).
- ²³O. Häusser, W. Witthun, T. K. Alexander, A. B. McDonald, J. C. D. Milton, and A. Olin, *Phys. Rev. Lett.* **31**, 323 (1973).
- ²⁴W. E. Frahn, *Phys. Rev. Lett.* **26**, 358 (1971); *Ann. Phys. (N.Y.)* **72**, 524 (1972).
- ²⁵R. Anni and S. Tobbara, *Riv. Nuovo Cimento* **3**, 1 (1970).
- ²⁶K. J. Le Couteur and D. W. Lang, *Nucl. Phys.* **13**, 32 (1959).
- ²⁷S. Cohen and W. J. Swiatecki, *Ann. Phys. (N.Y.)* **22**, 406 (1963).
- ²⁸S. Cohen, F. Plasil, and W. J. Swiatecki, *Ann. Phys. (N.Y.)* **82**, 557 (1974); see also C. E. Rosenkilde, *J. Math. Phys.* **8**, 98 (1967).
- ²⁹T. D. Thomas, *Phys. Rev.* **116**, 703 (1959).
- ³⁰J. Gilat, Brookhaven National Laboratory Report No. BNL 50246, 1970 (unpublished). See also J. R. Grover and J. Gilat, *Phys. Rev.* **157**, 802 (1967) and references therein.
- ³¹U. Mosel and H. W. Schmitt, *Phys. Lett.* **37B**, 335 (1971).